Solar Energy 187 (2019) 85–94

Contents lists available at ScienceDirect

Solar Energy

journal homepage: www.elsevier.com/locate/solener

High performance integrated receiver-storage system for concentrating solar power beam-down system

Song Yang[a], Jun Wang[a,*], Peter D. Lund[a,b], Chuan Jiang[a], Xiuxiu Li[a]

[a] Key Laboratory of Solar Energy Science and Technology in Jiangsu Province, Southeast University, School of Energy and Environment, No.2 Si Pai Lou, Nanjing 210096, PR China

[b] Aalto University School of Science, P.O. Box 15100, FI-00076 Aalto (Espoo), Finland

ARTICLE INFO

Keywords:
Concentrating solar power
Heat transfer
Thermal energy storage
Packed bed storage
Beam-down system
Thermocline

ABSTRACT

Concentrating solar power systems (CSP) with thermal storage units can provide dispatchable power. Here we propose a modified design of a cavity receiver combined with a thermocline heat storage unit for the beam-down CSP. Instead of using a separate receiver and heat storage unit, an integrated unit consisting of an extended cylindrical cavity with a packed bed storage is proposed. The new approach was designed using validated cavity radiation and quasi-1D 2-phase numerical heat transfer models. As the concentrated irradiation can be directly absorbed in such a system, the structure used can be simplified and operation of the unit is more effective. A high solar-to-exergy conversion ratio of 0.52 was reached with an optimized design, charging and discharging efficiencies being well beyond 99% and 92% at 770 °C. An important detail in the integrated receiver-storage design was the use of a circulation air flow fan, which enhanced the heat transfer inside the packed bed storage. The proposed design is promising for improving the efficiency and economics of beam down CSP.

1. Introduction

Concentrating solar thermal power (CSP) is a promising renewable energy technology, which can provide dispatchable power when connected to thermal energy storage (TES) (Kuravi et al., 2013). Therefore, developing efficient and cost-effective TES systems has high relevance for future CSP technologies (Pardo et al., 2014). Recent CSP projects seem to increasingly employ TES (Pelay et al., 2017).

The thermophysical principle of a thermal storage unit can be based on sensible heat, latent heat of fusion or vaporization, or on reversible chemical reactions (Kuravi et al., 2013). Sensible heat storage is so far the most commonly used approach because of simplicity and a wide range of low-cost materials available, though its transient heat transfer characteristics and total heat storage mass flux falls well behind the two other forms of TES (Pelay et al., 2017; Romero and Steinfeld, 2012). Typical sensible heat storage materials include e.g. rock gravel, sand or concrete (Brosseau et al., 2005; Tamme et al., 2004; Zanganeh et al., 2012), and for working fluid, molten salt, steam, or high temperature oil (Gil et al., 2010; Liu et al., 2016; Steinmann and Eck, 2006; Gil et al., 2010; Steinmann and Eck, 2006) have been used (Herrmann and Kearney, 2002; Medrano et al., 2010). Combining a packed bed of rocks as storage material and air as heat transfer fluid (HTF) has been proposed due to the inherent technical and economic advantages associated, such as abundant and economical storage material, no hazardous or corrosive ingredient, and direct heat transfer mode, etc. (Zanganeh et al., 2015a). Because of the attractiveness of rock as a storage material, the effects of high-temperature (up to 1000 °C) thermal cycling on rocks have received much attention in the past decades (Becattini, 2018). Good long-term stability of rock storage has been reported (Allen et al., 2014; Riaz, 1977; Tiskatine et al., 2016). Here we consider the same composition as used in a pilot-scale storage system (ETH), mainly containing Siliceous Limestone, Quartzite, Limestone, Calcareous Sandstone and Gabbro (Zanganeh et al., 2012).

In this paper, we present a cavity receiver integrated with a packed-bed rock storage as a thermal energy storage for a beam-down CSP system to simplify overall design and find more effective solutions for system design. It is well-known that packed beds have been subject to extensive general methodology development and analyses of specific cases in the past (Beek, 1962; Kunii and Smith, 1960, 1961; Pfeffer, 1964; Whitaker, 1972), but the literature on integrated receiver-storage is negligible. Examples of past work on packed-bed thermal storage include e.g. determining the effective thermal conductivity of porous rocks (Kunii and Smith, 1960, 1961), heat and mass transport in fixed beds (Beek, 1962; Pfeffer, 1964), correlations for heat transfer (Whitaker, 1972), heat transfer models for high porosity and complex micro-structure cases (Kaviany, 2012), determining radiative transport properties of porous media (Ganesan and Lipiński, 2011; Petrasch et al., 2007), and different 1D-3D models for performance analysis of packed

* Corresponding author.

https://doi.org/10.1016/j.solener.2019.05.041
Received 7 April 2019; Received in revised form 16 May 2019; Accepted 17 May 2019

Nomenclature

Symbols

C	concentration ratio or specific area (– or m^2/m^3)
c_p	specific heat (J/kgK)
d	effective diameter of rocks (m)
F	view factor matrix
H	height (m)
h	specific enthalpy (J/kg)
h_{rs}	void to void radiative heat transfer coefficient (W/m^2K)
h_{rv}	solid surface to solid surface radiative heat transfer coefficient (W/m^2K)
k	thermal conductivity (W/mK)
L	thickness (m)
$\dot{m}$	mass flow rate (kg/s)
Nu	Nusselt number (–)
Pr	Prandtl number (–)
p	pressure (Pa)
Q	thermal energy (MWh)
$\dot{Q}$	heat flux (kW)
Re	Reynolds number (–)
q	irradiation (W/m^2)
$\bar{q}$	average irradiation (W/m^2)
R	radius (m)
t	time (s)
T	temperature (K\˚C)
U	overall heat transfer coefficient (W/m^2K)
α	rim angle (˚)
β	constant
γ	circulation flow to output flow ratio (–)
δ	Dirac delta function
ε	porosity (–)
ΔT	temperature difference (K\˚C)
$\bar{T}$	integral mean of temperature (K\˚C)
ϵ	emissivity (–)
η	efficiency (%)
Θ	non-dimensional temperature (–)
ν	viscosity (m^2/s)
ξ	solar to exergy conversion ratio (–)
ρ	density (kg/m^3)
σ	Stefan-Boltzmann constant or RMSE (W/m^2K^4 or m)
σ_T	relative deviation of outlet temperature during discharging (%)
ϕ	constant
$\|\|$	absolute value

Subscripts

0	initial or original point
absorb	absorbing
bottom	bottom
c	charging
cav	cavity
conv	convective
cycle	charging-discharging cycle
d	discharging
eff	effective
f	fluid
fan	fan
inc	incident
inlet	inlet to the discharging phase
inside	inside wall
layer	layer of storage
loss	loss
max	max
net	net
outlet	outlet to the discharging phase
rad-cond	radiative and conductive
s	solid
storage	storage
surf	cavity surface
top	top
ν	volumetric
w	wall
∞	ambient

Abbreviations

CPC	compound paraboloid concentrator
CSP	concentrated solar power system
CT	computer tomography
EP	equilibrium point
HTF	heat transfer fluid
IRS	integrated receiver-storage system
LDC	low-density concrete
RPC	reticulate porous ceramic
STS	spatially thermal stratification
TES	thermal energy storage
UPC	ultra-high-performance concrete
VF	view factor

beds (Geissbühler et al., 2016; Ismail and Stuginsky, 1999; Meier et al., 1991; Zanganeh et al., 2014b; Zanganeh et al., 2015a; Zanganeh et al., 2015b; Zanganeh et al., 2012; Zavattoni et al., 2015), among others. Besides, packed-bed has been widely applied in high-temperature solar receiver/reactor systems to obtain a high heat/mass transfer rate (Chueh et al., 2010; Furler and Steinfeld, 2015; Hischier et al., 2012; Keene et al., 2013). To date, the studies in terms of thermocline heat storage for solar tower and dish power systems have mainly focused on the sensitive and latent heat transfer issues (Geissbühler et al., 2016; Zanganeh et al., 2014b; Zanganeh et al., 2015a; Zanganeh et al., 2015b; Zanganeh et al., 2012). The merit of the proposed integrated receiver-storage design lies in the possibility to eliminate heat exchangers as well as complex connecting devices. Thus, a simplified structure and operation is possible, which could reduce overall costs, improve system stability, and lead to high heat transfer efficiency.

In present work, the cavity receiver integrated with a packed-bed as the thermal storage is intended for a beam-down CSP system. The concept of beam-down was initially suggested in 1970s for central receivers (Rabl, 1976), and it has been further developed theoretically and experimentally for different designs (Segal and Epstein, 1999; Segal and Epstein, 2001; Vant-Hull, 2014). Using a secondary reflector in this context enables to place the heavy components at ground level, thus enabling simpler and cheaper tower and heat transport sub-systems (Vant-Hull, 2014). Also, the concentration ratio can be improved through shortening the optical path. A few beam-down systems have been built so far (Matsubara et al., 2014; Mokhtar et al., 2014), but applications of interest include fuel production via thermochemical reactions (Furler and Steinfeld, 2015) or power generation integrated with thermal storage systems (Koepf et al., 2012; Matsubara et al., 2014; Tamaura et al., 2006). Hence, the proposed integrated receiver-storage (IRS) design with a beam-down CSP has high relevance.

To our best knowledge, the original concept of the IRS for CSP was initially proposed by Slocum et al. in 2011 (Slocum et al., 2011). In their work, a CSP system with integral storage was presented, where

heliostats direct sunlight into a volumetric absorption molten salt receiver. The incident concentrated sunlight can therefore be directly absorbed when penetrating the salt. Here we employed a modified IRS design to achieve a direct absorption of solar radiation for a beam-down CSP system. Different from Slocum's design, we considered a packed bed as the storage media and air as HTF instead of molten salt aiming for simplifying the system and reducing operating complexity. Also, a novel recirculation device was designed to enhance the heat transfer inside the bed.

The paper is organized as follows. In Chapter 2, we describe the modified receiver-storage design, in Chapter 3 the methodology for modelling the design including the validation of the simulation model, in Chapter 4 we present the main results, and finally in Chapter 5 the conclusions.

2. Description of the modified receiver-storage design

In this section, the technical details for the integrated receiver-storage system (IRS) are given, which are later used in the simulations and analyses. The basic CSP considered is a 450 kW_{th} beam-down system located in eastern China with an average normal radiation (DNI) of 4.8 kWh/m^2 per day. The daily storage capacity of the IRS is designed as 2 MWh_{th}. Total optical efficiency and average concentration ratio (C) are set to 63% and 900 suns, considering the state-of-the-art of the commercial heliostats and central reflectors (reflectivity 0.8 and 0.95, mirror error 1 mrad) and tracking accuracy (~2.5 mrad) (Mokhtar et al., 2014; Wei et al., 2013). Fig. 1 shows a sketch of the IRS and its working principle. The operating process is as follows: at the beginning of charging of the TES, the top of the packed bed is exposed to concentrated solar irradiation and heated up from the initial temperature. Cooler air is pumped out by M_1 from the bottom of the storage, while another fan (M_2) is used to circulate the top air flow for enhancing heat exchange within the bed. The Model AFP® produced by Daniels Fans© was available for M_2 which can circulate the high temperature air (up to 950 °C) in a controllable volumetric flow rate (up to 50 m^3/s) (DanielFans). The power of M_1 and M_2 are subject to the desired output temperature of the HTF as well as the scale of the IRS. The charging mass flow rate of M_1 ($\dot{m}_{1c}$) is fixed to 0.4 kg/s while the rate of circulation air ($\dot{m}_{2c}$) varies in the range of 0–4 kg/s. Here we define the circulation flow to output flow ratio as $\gamma = \dot{m}_{2c}/\dot{m}_{1c}$, which indicates the relation of the mass flow rates, i.e. the powers, offered by M_1 and M_2. The charging time is set here to 8 h (daytime). During the discharge, air flows through the packed bed inversely and exits from the outlets arranged on the side walls of cavity. The discharging mass flow rate of M_1 ($\dot{m}_{1d}$) is fixed to 0.2 kg/s. The aperture is closed so that hot air cannot escape from the top. The discharge time is set to 16 h (night-time). Metal grids are used for eliminating heterogeneity of flow velocity at the same cross section due to the fan effect.

The tank is immersed in the ground (except for the cavity part) for reducing the lateral load bearing caused by the expanding rock during a charge half-cycle as well as heat losses. It has a cylindrical cross section with an inner radius of R_2 and a total height of $H_1 + H_2$. The insulation of the cavity contains two layers: Al_2O_3–SiO_2 (inner) and Foamglass® (outer) with a total thickness of L_1 for the lid and L_2 for the side. It is enclosed outside with a thin layer of Inconel 600. The immersed part of the tank is made of insulation (2 layers) and concrete (2 layers): Microtherm®, Foamglas®, ultra-high-performance concrete (UPC) and low-density concrete (LDC) (Martinola et al., 2010). The thicknesses of the base and side wall are L_3 and L_4, correspondingly. The packed bed is filled with rocks till the ground level. The equivalent thermal properties and geometries are selected here according to the characteristics of rocks (Somerton, 1992; Zanganeh et al., 2015a; Zanganeh et al., 2012). Specific heat and thermal conductivities are plotted in Fig. 2 as a function of temperature. The inlets of M_2 are inserted from the side at a height of H_3 beneath the ground for transporting air back to the cavity. Not shown in Fig. 1, but four symmetric inlets are designed along the lateral walls for reducing the effect of the air bypass. The aperture of cavity is R_1. A compound paraboloid concentrator (CPC) is coupled with the IRS configuration to improve the concentration ratio up to 900. The details of the design are shown in Tables 1 and 2. It is worth noting that thermal ratcheting may occur when a tank filled with particulate solids is heated and cooled successively (Flueckiger et al., 2011; Kolb et al., 2011). Two conditions should be considered: (1) if the tank wall expands more than the filled particles a gap may form and then the particles may subside to fill the gap. When the tank is cooled, however, the wall contracts against the bed and may experience stresses in excess of the yield stress, resulting in plastic deformation. Cyclic operations repeats the process and the tank wall is slowly "ratcheted" outward until it fails; (2) conversely, if the bed expands more than the tank walls, it may deform the walls plastically on heat up. Ultimately over

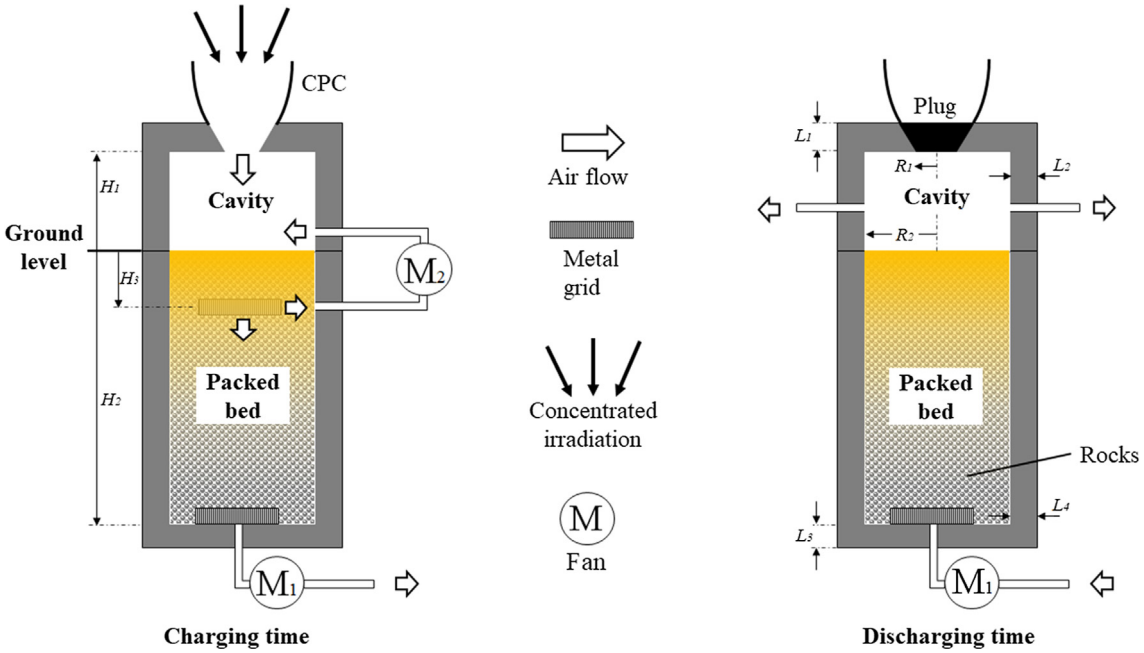

Fig. 1. Scheme of the integrated receiver-storage (IRS) configuration.

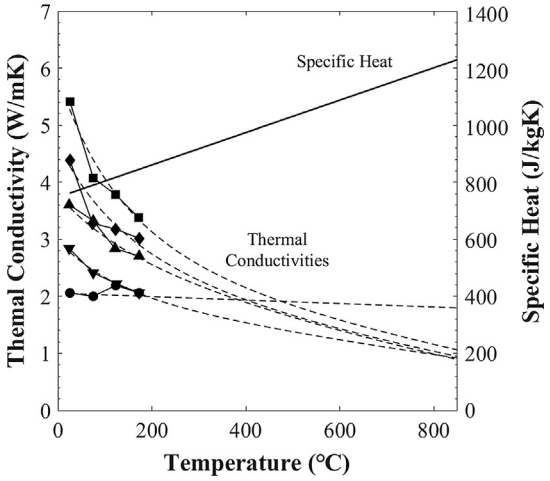

Fig. 2. Thermal conductivity and specific heat of the rocks as a function of temperature. Dashed lines: Extrapolations obtained using the correlations for thermal conductivity (Somerton, 1992) and specific heat (Zanganeh et al., 2015a). Solid lines: experimental data (Zanganeh et al., 2012) corresponding to ■ Quartzite, ◆ Calcareous Sandstone, ▲ Helvetic Siliceous Limestone, ▼ Limestone, and ● Gabbro.

Table 1
Dimensions and operating conditions of the integrated receiver-storage system (IRS) design.

Dimensions		Operating conditions	
H_1 (m)	1.5	charging time, t_c (s)	28,800
H_2 (m)	8	discharging time, t_d (s)	57,600
H_3 (m)	0.33–1.65	HTF's outlet mass flow rate during charging, $\dot{m}_{1c}$ (kg/s)	0.4
R_1 (m)	0.447	HTF's outlet mass flow rate during discharging, $\dot{m}_{1d}$ (kg/s)	0.2
R_2 (m)	2	HTF's circulating mass flow rate during charging, $\dot{m}_{2c}$ (kg/s)	0–4
L_1 (m)	0.2/0.5	Circulation flow to output flow ratio, γ (–)	0–10
L_2 (m)	0.2/0.5	incident radiation flux, $\dot{Q}_{inc}$ (kW)	439.8
L_3 (m)	0.3/0.5/0.02/1	initial temperature, T_0 (K)	298
L_4 (m)	0.3/0.5/0.02/1	ambient temperature, T_∞ (K)	293
d (m)	0.003	efficiency of fan, η_{fan} (–)	0.95
ε (–)	0.342	solar-to-power efficiency of commercial CSP, η_{CSP} (–)	0.23

many cycles, failure of the tank could occur. Our specific design here is supposed to mitigate thermal ratcheting. In fact, the effect of the lateral earth pressure prevents the buried tank wall from expanding outward in a charge half-cycle. Moreover, the UPC can bear a high pressure while the soft structure of Microtherm® and Foamglas® as the buffered liner offers additional volume for the expanding bed. Therefore, the phenomena may not occur in our IRS system. A 3-D thermos-mechanical analysis would be necessary for an accurate evaluation, which was out of the scope of this paper.

3. Modelling of the integrated receiver-storage system

To analyze and optimize the thermal performance of the integrated receiver-storage system, we developed a thermal simulation model for the cavity receiver and the packed-bed storage. The basic assumptions made in the modelling were the following:

- All materials are isotropic and the surfaces are opaque gray-diffuse;
- Ambient temperature is set at 293 K and the sky is regarded as a black-body at an 8 K lower temperature (T_{sky} = 285 K) (Kalogirou, 2012);
- Conductive losses through insulation are 1-dimensional;
- For the discharging phase, the conductive heat losses to the cavity part (above the ground) are very small and can be ignored;
- A Gaussian distribution is used for incident solar radiation at the cavity bottom;
- Air is regarded as a non-radiative media except for the effect of void-to-void radiative heat transfer;
- A plug flow in the packed-bed so that the air mass flow rate is uniform at any cross-section perpendicular to the packed bed;
- Radial temperature differences are ignored for the packed bed;
- For the storage, the thermal inertia of the walls and the soil insulation layer is not considered.

3.1. Thermal model for the cavity receiver

Firstly, the net irradiation flux at the receiver bottom was modelled using Monte Carlo ray-tracing to obtain the matrix of the view factor (VF) for each surface element of the cavity inner walls. 1 *billion* photons were used to determine the VF matrix. The inner walls of the receiver were divided into a number of discrete meshes (N_{surf}). The number of nodes in radial, axial and circumferential directions were set to 50, 20, and 20 respectively. The insulation is also divided into 20 layers for solving the heat conduction. Then, the radiosity method was used to get the net irradiation flux at the cavity bottom by solving the set of equations below (Yang et al., 2018):

$$\sum_{j=1}^{N_{surf}} (\delta_{kj} - (1-\epsilon_j)F_{kj})\frac{q_{net,j}}{\epsilon_j} = q_{inc,k} - \sum_{j=1}^{N_{surf}} (\delta_{kj} - F_{kj})\sigma T_j^4 \quad (1)$$

where $q_{inc,j}$ and $q_{net,j}$ represent the incident solar irradiation and the net radiative heat flux at the j^{th} segment. ϵ is the emissivity, σ is Stefan-Boltzmann constant (5.6704×10^{-8} W/m^2 K^4), δ is the Dirac delta function, and F_{kj} is the VF from the k^{th} to the j^{th} segment.

In our case, the incident solar irradiation can just cover the cavity bottom with the special geometric design. It is assumed to obey a 2-D Gaussian distribution or 1-D Rayleigh distribution (Eq. (2)) with some constraints (Eq. (3)):

$$\frac{q_{inc}(r,\varphi)}{q_0} = e^{-\frac{r^2}{2\sigma^2}} \quad (0 \leqslant r \leqslant \infty,\ 0 \leqslant \varphi \leqslant 2\pi) \quad (2)$$

$$\frac{q_{inc}(R_2,\varphi_0)}{q_{inc}(0,\varphi_0)} = \frac{1}{e^2};\quad and \quad \bar{q}_{inc} = \frac{\int_0^{2\pi}\int_0^{R_2} q_{inc}(r,\varphi) r dr d\varphi}{\pi R_2^2} \quad (3)$$

where q_0 is the peak value of q_{inc} (r = 0 m) and $\bar{q}_{inc}$represents the average incident solar irradiation, set as 3.5×10^4 W/m^2 here. Thus, $\sigma = \frac{R_2}{2}$ and $q_0 = \frac{R_2^2 \bar{q}_{inc}}{2\sigma^2\left(1 - e^{-\frac{R_2^2}{2\sigma^2}}\right)}$.

To match the scale of $\bar{q}_{inc}$, the HTF's mass flow rates of charging ($\dot{m}_{1c}$) and discharging ($\dot{m}_{1d}$) are set as 0.4 kg/s and 0.2 kg/s, respectively. The operating temperature can be fixed in the interesting range of 500–800 °C by optimizing the circulating mass flow rate ($\dot{m}_{2c}$).

The concentration ratio (C) of 900 *suns* was chosen based on the technical status of beam down systems (Wei et al., 2013). The rim angle of the concentrating sunlight (α) is set as 53°. DNI = 800 W/m^2. Therefore, $H_1 = \frac{R_2}{\tan\alpha}$ and $R_1 = R_2\sqrt{\frac{\bar{q}_{inc}}{C \cdot DNI}}$. H_2 is fixed as the minimum height ensuring the temperature of the bed's bottom close to the surroundings ($(T_{s,f}(z = H_2) - T_\infty)_{\max} < 10$ K). The dimensions of the IRS are shown in Table 1.

The net radiative heat flux (q_{net}) in Eq. (1) is calculated sequentially according to the temperature of the cavity bottom, i.e. the surface of the storage, varying from the initial value (T_0) to the maximum (T_{max}) corresponding to the initial and steady states. Since the q_{net} consists of two parts, the heat flux losses from the cavity walls (q_{loss}), and the energy absorbed by the cavity bottom (q_{absorb}). Therefore, the q_{absorb} can be obtained from q_{net} minus q_{loss} and finally be fitted as a 3-order

Table 2
Main physical properties of materials used in the IRS (Furler and Steinfeld, 2015; Kelley, 1960; Somerton, 1992; ToolBox, 2005; Yang et al., 2018; Zanganeh et al., 2015a; Zanganeh et al., 2012).

Material	Conductivity & Specific heat & Viscosity & Density & Emissivity k (W/mK) & c_p (J/kgK) & ν ($\times 10^6$ m^2/s) & ρ (kg/m^3) & ϵ (–)
Rocks (Kelley, 1960; Somerton, 1992; Zanganeh et al., 2015a; Zanganeh et al., 2012)	$k(T) = \begin{cases} k_{20} - A(T-B)(k_{20}-C)\left[k_{20}(DT)^{-Ek_{20}} + F\right] k_{20}^{-G} & k_{20} > 2W/mK \\ k_{20} - A(T-B)(k_{20}-C) & k_{20} < 2W/mK \end{cases}$ $c_p(T) = 747.0995 + 0.5676 \times (T - 273)$ $\rho = 2732.6$ $\epsilon = 0.85$
Air (ToolBox, 2005; Yang et al., 2018)	$k(T) = 2.35 \times 10^{-12}T^3 - 1.290 \times 10^{-8}T^2 + 4.8370613 \times 10^{-5}T + 0.00483$ $c_p(T) = 1171 \times e^{-\left(\frac{T-3070}{2257}\right)^2} + 691.6 \times e^{-\left(\frac{T-516.2}{1673}\right)^2} + 191 \times e^{-\left(\frac{T+114.3}{399.4}\right)^2}$ $\nu(T) = 258.7 - 259.4\cos(0.001214T) - 88.17\sin(0.001214T) - 6.35\cos(0.002428T) + 49.59\sin(0.002428T) - 5.995\cos(0.003642T) - 0.2957\sin(0.003642T)$ $\rho(T) = 352.6T^{-0.9998} - 1.747 \times 10^{-4}$
Al_2O_3–SiO_2 (Furler and Steinfeld, 2015)	$k(T) = 0.00012926T + 0.019654$ $c_p(T) = \min\{4 \times 10^{-7}T^3 - 1.3797 \times 10^{-3}T^2 + 1.5987289T + 477.6995948, 1118.44\}$ $\rho = 560.65$ $\epsilon = 0.85$
Insulation (Zanganeh et al., 2012)	$k = 0.025/0.05/2.05/0.375/0.5$ (*Microtherm®/Foamglas®/UPC/LDC/Soils*) $c_p = 840$ (*Foamglas®*) $\rho = 115$ (*Foamglas®*) ϵ(T) = 0.0001982 × T + 0.5734(Inconel 600)

polynomial function of the temperature (Eq. (4)):

$$q_{absorb}(T) = AT^3 + BT^2 + CT + D \tag{4}$$

A, B, C and D are equal to -1.246×10^{-5}, 0.0148, −7.434 and 3.572×10^4 in this case.

3.2. Heat transfer model for the packed bed

Next, a quasi 1-D two-phase numerical transient heat transfer model for the storage is presented. Air and solid phase are separately modelled in the same 1-D space based on the law of energy conservation (Eqs. (5) and (6)):

$$\text{Solid phase:}\quad \frac{\partial((1-\varepsilon)\rho_s c_{ps} T_s)}{\partial t} = \frac{\partial}{\partial z}(k_{eff}\frac{\partial T_s}{\partial z}) + h_v(T_f - T_s) + q_v\delta(z-0) \tag{5}$$

$$\text{Fluid phase:}\quad \frac{\partial(\varepsilon\rho_f c_{pf} T_f)}{\partial t} + \frac{\partial(c_{pf}\dot{m}_f T_f)}{\partial z} = h_v(T_s - T_f) + U_w C_w(T_\infty - T_f) \tag{6}$$

Boundary conditions:

$$\text{Charging:}\quad \begin{aligned} &T_f(t>0, z=0) = f^{-1}\left[\frac{h_{f,0} + \gamma h_f(t>0, z=H_3)}{1+\gamma}\right]; \\ &\frac{\partial T_f(t>0, z=H_2)}{\partial z} = 0; \\ &q_v = -\frac{dq_{absorb}}{dz}; \\ &\frac{\partial T_s(t>0, z=H_2)}{\partial z} = 0. \end{aligned} \tag{7}$$

$$\text{Discharging:}\quad \begin{aligned} &T_f(t>0, z=H_2) = T_0; \\ &\frac{\partial T_f(t>0, z=0)}{\partial z} = 0; \\ &\frac{\partial T_s(t>0, z=0)}{\partial z} = 0; \\ &\frac{\partial T_s(t>0, z=H_2)}{\partial z} = 0. \end{aligned} \tag{8}$$

$$\text{Initial conditions:}\quad T_f(t=0, 0<z<H_2) = T_s(t=0, 0<z<H_2) = T_0. \tag{9}$$

Eqs. (5) and (6) are discretized with the Euler explicit method in time and with the second order central difference in space and can then be written as follows:

$$\begin{aligned} &(1-\varepsilon)\rho_s c^i_{ps,n}\frac{T^{i+1}_{s,n} - T^i_{s,n}}{\Delta t} \\ &= \frac{k^i_{eff,n}(T^i_{s,n+1} - T^i_{s,n}) - k^i_{eff,n-1}(T^i_{s,n} - T^i_{s,n-1})}{\Delta z^2} + h^i_{v,n}(T^i_{f,n} - T^i_{s,n}) + q^i_{v,n} \end{aligned} \tag{10}$$

$$\begin{aligned} &\varepsilon\rho^i_{f,n} c^i_{pf,n}\frac{T^{i+1}_{f,n} - T^i_{f,n}}{\Delta t} + \dot{m}_f c^i_{pf,n}\frac{T^i_{f,n} - T^i_{f,n-1}}{\Delta z} \\ &= h^i_{v,n}(T^i_{s,n} - T^i_{f,n}) + U^i_{w,n} C_w(T_\infty - T^i_{f,n}) \end{aligned} \tag{11}$$

An optimal grid spacing of 0.066 m is chosen as this gave a good accuracy with relatively low computing cost. Compared to the fine grid spacing of 0.006 m, the relative variance (Eq. (12)) is less than 10^{-3}.

$$\frac{\sum_{Layer}(result|_{Optimal\ grid} - result|_{Fine\ grid})^2}{\sum_{Layer}(result|_{Fine\ grid})^2} < 10^{-3} \tag{12}$$

where *result* represents the solid or fluid temperature of each layer after charging or discharging.

Numerical stability analysis was ensured by two criteria of the solid and air phases given in Eq. (13). Time step of 0.01 s (charging) and 0.02 (discharging) is used to ensure stability.

$$\begin{cases} 1 - \frac{(k^i_{eff,n} + k^i_{eff,n-1})\Delta t}{(1-\varepsilon)\rho_s c^i_{ps,n}\Delta z^2} - \frac{h^i_{v,n}\Delta t}{(1-\varepsilon)\rho_s c^i_{ps,n}} > 0 \\ 1 - \frac{\dot{m}_f \Delta t}{\varepsilon\rho^i_{f,n}\Delta z} - \frac{h^i_{v,n}\Delta t}{\varepsilon\rho^i_{f,n} c^i_{pf,n}} > 0 \end{cases} \tag{13}$$

In Eq. (7), the specific enthalpy of the fluid phase is defined as $h_f = \int_{T_{ref}}^{T} c_{pf}(T)dT$, and the temperature of the mixed input air during charging is calculated from $T_f = f^{-1}(h_f)$.

3.2.1. Effective conductivity of packed bed (k_{eff})

Because of the high temperature of charging and temperature gradient in the axial direction, the correlation of Kunii and Smith (Kunii and Smith, 1960; Yagi and Kunii, 1957) in Eq. (14) is applied to calculate the effective conductivity of packed bed, k_{eff}, which considers the thermal conductivity of both the solid and the fluid, as well as the radiative transfer, including the void to void radiative heat transfer coefficient (h_{rv}) and the solid surface to solid surface radiative heat

transfer coefficient (h_{rs}):

$$k_{eff} = k_f \left[\varepsilon \left(1 + \beta \frac{h_{rv} d}{k_f} \right) + \frac{\beta(1-\varepsilon)}{\frac{1}{\frac{1}{\phi} + \frac{h_{rs} d}{k_f}} + \frac{2}{3}\left(\frac{k_f}{k_s}\right)} \right]; \tag{14}$$

where $\phi = \phi_2 + (\phi_1 - \phi_2)\frac{\varepsilon - \varepsilon_2}{\varepsilon_1 - \varepsilon_2}$ ($\varepsilon_1 = 0.476$, $\varepsilon_2 = 0.26$), $\phi_i = \frac{1}{2}\frac{\frac{k_s - k_f}{k_s}\frac{1}{n_i}}{\ln\left(\frac{k_s}{k_f} - \frac{k_s - k_f}{k_f}\sqrt{1 - \frac{1}{n_i}}\right) - \frac{k_s - k_f}{k_s}\left(1 - \sqrt{1 - \frac{1}{n_i}}\right)} - \frac{2}{3}\frac{k_f}{k_s}$ ($n_1 = 1.5$, $n_2 = 4\sqrt{3}$),

$h_{rv} = \frac{3.4424\sigma T_f^3}{1 + \frac{\varepsilon}{2(1-\varepsilon)}\frac{1-\epsilon_s}{\epsilon_s}}$, $h_{rs} = 3.4424\left(\frac{\epsilon_s}{2-\epsilon_s}\right)\sigma T_s^3$.

β is constant equal to 0.9 in our case. Note that the non-uniform radial distribution or "the wall effect" can be neglected due to the large tank to rock diameter ratio (> 40) (Meier et al., 1991).

3.2.2. Volumetric solid-fluid convective heat transfer coefficients (h_v)

Various rock-to-fluid convective heat transfer correlations have been proposed for different flow conditions (Alanis et al., 1977; Coutier and Farber, 1982; Löf and Hawley, 1948; Pfeffer, 1964). It has been found that h_v may significantly affect the final results. Therefore, the correlations should be chosen with care corresponding to the operating conditions in each case. In our case the model by Alanis et al. and Coutier & Farber (Eq. (15)) was found proper:

$$h_v = l_m(\dot{m}/d)^{l_n} \tag{15}$$

where l_m and l_n depends on the Reynolds number (Table 3).

3.2.3. Overall wall heat transfer coefficient (U_w)

For the lateral insulation of tank, the overall heat transfer coefficient is calculated as:

$$U_w = \frac{1}{\frac{1}{U_{inside}} + R_2 \sum_{j=1}^{n} \frac{1}{k_j} \ln \frac{r_{j+1}}{r_j}} \tag{16}$$

$$U_{inside} = h_{conv,w} + h_{rad-cond,w} \tag{17}$$

$$h_{conv,w} = \frac{k_f}{d}[3.22(RePr)^{1/3} + 0.117Re^{4/5}Pr^{2/5}] \tag{18}$$

$$h_{rad-cond,w} = \frac{k_{eff,w}}{R_2 \ln \frac{R_2}{R_2 - d/2}} \tag{19}$$

The insulation consists of Microtherm®, Foamglas®, UPC, LDC, and soil with thicknesses given in Table 1 and conductivities in Table 2. $1/U_{inside}$ represents the heat resistance between the packed bed (including the fluid) and inner laterals wall, which mainly consists of the convective effect from the fluid phase and the radiative-conductive effect from the solid phase. $h_{conv,w}$ and $h_{rad\text{-}cond,w}$ accounts for the convection and the radiation-conduction terms calculated with Eq. (18) (Beek, 1962) and Eq. (19), correspondingly. Re in Eq. (18) is calculated by $\dot{m}d/(\rho\nu)_f$. $k_{eff,w}$ in Eq. (19) is obtained from correlations given by (Ofuchi and Kunii, 1965) which is similar to Eq. (14).

3.3. Validation of the models

The thermal model for cavity receiver has been validated in our previous work (Yang et al., 2018). In this paper we therefore focus on demonstrating the validity of the heat transfer model for the packed bed. The case of an industrial thermal storage system for a 26 MWe CSP plant in Morocco is used here for the validation. This case differs from our design in that the storage is charged by hot air instead of solar irradiation. The dimensions and operating conditions are given in Table 4. The rest of the parameters are the same as in our case (Table 1). We simulated a 30-days period with our in-house code and compared the results to Zanganeh's numerical results which have been verified against experiments (Zanganeh et al., 2012). Fig. 3 presents the non-dimensional temperature (Θ) of outlet air after each cycle and the solid phase temperature distribution vs height after charging and discharging of 1, 10, 20, and 30 cycles (1 cycle = 1 day). The agreement of the results is good.

4. Results and discussion

The performance of the IRS system is assessed in the following aspects: spatial thermal stratification (STS), transient outlet air temperature during discharging (T_{outlet}), cavity absorbing heat efficiency (η_{absorb}), charging and discharging efficiencies ($\eta_{charging}$, $\eta_{discharging}$), and the total solar-to-exergy conversion ratio (ξ_{cycle}). The results are presented in detail in the next.

4.1. Thermal characteristics of the IRS

In the proposed design, the incident beam directly strikes on the first layer of the packed bed. Air is forced to sweep through the bed from the top towards the down carrying heat to the lower layers. The thermocline of the IRS after the charging and discharging phases is illustrated in Fig. 4. It corresponds to the 15th cycle with $\gamma = 6$ and $H_3 = 0.33$ m. The temperature distribution of the packed bed after discharging is similar to that of the fluid phase fitting the general Gaussian equation (Fig. 4a). The temperature decays in axial direction (z) as e^{-z^2}. In the solid phase, the highest temperature is reached at the top due to the heating effect of direct solar irradiation. The temperature drops when moving downwards and approaches an inflection point at $z < H_3$. The rest of the thermocline follows the Gaussian distribution. For the fluid phase, the temperature in the first layer is lower and increases to the peak then gradually decreases with z. The distribution is similar to that of the packed bed when $z > H_3$. The point (marked with a dotted circle in Fig. 4b) is called the equilibrium point (EP), where the temperature of two phases are identical. Above the EP, the air is at relatively lower temperature than the packed-bed and it thus absorbs heat from the packed bed. Inversely, the heat is released from air and stored in the bed below the EP.

The temperature evolution of 1st layer of the packed bed (T_{layer1}) is also presented for demonstrating the charging-discharging performance during multi-cycle performance. Fig. 5 depicts the curve of T_{layer1} against time within 15 cycles. The mean of T_{layer1} is also shown. The triangle and circle markers correspond to the charging and discharging phases, respectively. The oscillation of temperature is rather intense at the start-up stage but then decreases rapidly during the first ~5 cycles. After 30 cycles, the mean temperature of the charging and discharging periods approach steady-state values of 884 °C and 766 °C in this case.

4.2. Reheat effect

In the present design, air fan M_2 plays an important role on the performance of the thermal storage due to the reheat effect (Fig. 1) as a certain amount of air flow can be reheated through the reflow. Next, we mainly discuss the impacts of the circulation flow ratio (γ) and the circulation flow length (H_3). Table 5 shows the effects of these parameters; a more detailed discussion in given in Sections 4.2.1 and 4.2.2.

4.2.1. Effect of circulation flow ratio (γ)

The amount of solar thermal energy absorbed by the storage

Table 3
Coefficients for volumetric convective heat transfer correlation.

	l_m	l_n
Small Reynolds number (< 50) (Coutier and Farber, 1982)	700	0.76
Large Reynolds number (50–400) (Alanis et al., 1977)	824	0.92

Table 4
Main parameters of the case for the validation of the model.

Dimensions		Operating conditions	
R_{top} (m)	20	$\dot{m}_c$ (kg/s)	132
R_{bottom} (m)	16	$\dot{m}_d$ (kg/s)	66
H (m)	25	T_c (°C)	650
d (m)	0.03	T_d (°C)	150

(Q_{absorb}), the outlet flow temperature ($T_{outlet,\min\backslash\max}$, ΔT_{outlet} and $\bar{T}_{outlet}$) and the relative temperature deviation ($\sigma_T = \frac{T_{outlet} - \bar{T}_{outlet}}{\bar{T}_{outlet}} \times 100\%$) during discharging are considered here for assessing the impact from γ. Here $T_{outlet,\min\backslash\max}$, ΔT_{outlet} and $\bar{T}_{outlet}$ represent the extremes, the difference, and the integral mean value of the outlet flow temperature, respectively. H_3 is set as 0.33 m and γ varies from 0 to 10 as shown in Table 5. Fig. 6a shows the simulated results at the end of the 30th cycle. Q_{absorb} and $\bar{T}_{outlet}$are relatively low (2.35 MWh and 653 °C) when γ = 0. A clear improvement is found at γ ~ 6. The temperature gap (ΔT_{outlet}) decreases as well. Beyond γ = 6 the values stabilize explained by the heat transfer enhancement between the packed bed and air when using the reflowing air fan M_2. Thus, a lower ΔT_{outlet} and a higher $\bar{T}_{outlet}$ can be reached. Meanwhile, for the reason, $|\sigma_T|$ can be also reduced at the later stage of discharging. Fig. 7a presents $|\sigma_T|$ drops down to 5.2% from 10.2% at the end of the 30th cycle when increasing γ from 0 to 8. Due to the limitations in the geometry and materials, the thermal storage approaches this optimal stage after increasing γ.

4.2.2. Effect of circulation flow length (H_3)

Next we consider the effects of the circulation flow length (H_3) by fixing γ = 4 and varying H_3 from 0.33 to 1.65 m. The simulation results of the 30th cycle are given in Fig. 6b. The effect of H_3 on the amount of absorbed heat is very limited. Q_{absorb} increases by 1.1% only when quintupling H_3. However, ΔT_{outlet} is furthered decreased from 131 to 74 °C as the circulation length is broadened from 0.33 m to 1.65 m under the same flow ratio value. $\bar{T}_{outlet}$ barely changes with H_3. The peak value 760 °C is obtained with H_3 = 1.32 m. Note that $T_{outlet,\min}$ gets closer to $\bar{T}_{outlet}$when increasing H_3, because attenuation of T_{outlet} at later stage of discharging improves. The $|\sigma_T|$ is < 2.5% when H_3 > 0.99 m (Fig. 7b), which is crucial to the operation of the power block. The effect is positively correlated to H_3 and stabilizes after $H_3 = H_2/8$.

Summarizing, the performance of the thermal storage can be improved either through increasing the circulation flow rate or the circulation flow range. But, meanwhile, the room for improvement is also limited by the other factors such as the geometry and materials. Eventually, the limit is supposed to be approached when the values of γ and H_3 are large enough, corresponding to 6 and 1 m in this case. It will be further discussed in terms of the local efficiencies and total conversion ratio in the last section.

4.3. Efficiency of the IRS

The amount of heat obtained during absorbing, charging, and discharging can be calculated from the following equations:

$$Q_{absorb} = \int_0^{t_c} \pi R_2^2 q_{absorb}\, dt \tag{20}$$

$$Q_{charging} = \int_0^{t_c} \int_0^{H_2} \pi R_2^2 (1-\varepsilon)\rho_s c_{ps} T_s\, dz dt \tag{21}$$

$$Q_{discharging} = \int_0^{t_d} \int_{T_{inlet}}^{T_{outlet}} \dot{m}_d c_{pf}\, dT dt \tag{22}$$

Then, the thermal efficiencies and the solar-to-exergy conversion ratio can be defined by Eqs. (23)–(26):

$$\eta_{absorb} = \frac{Q_{absorb}}{\dot{Q}_{inc} \cdot t_c} \tag{23}$$

$$\eta_{charging} = \frac{Q_{charging}}{Q_{absorb}} \tag{24}$$

$$\eta_{discharging} = \frac{Q_{discharging}}{Q_{charging}} \tag{25}$$

$$\xi_{cycle} = \frac{\int_0^{t_d} \left(\int_{T_{inlet}}^{T_{outlet}} \dot{m}_d c_{pf}\, dT \right) \left(1 - \frac{T_\infty}{T_{outlet}}\right) dt}{\dot{Q}_{inc} \cdot t_c} \tag{26}$$

Fig. 8 illustrates the these parameters during a 30-days' operation. For the start-up phase, $\eta_{discharging}$ is quite low, but after 10 cycles it rapidly climbs from 47.2% to 86.2%. As a result, the exergic conversion ratio improves from 0.27 to 0.50. However, η_{absorb} and $\eta_{charging}$ still drop during this interval, which is mainly because the heat loss through the aperture and the insulation is increasing as thermal energy is gradually accumulating and stored in the packed bed. Eventually, the storage approaches a steady cyclic behavior after 30 cycles and the ξ_{cycle} is > 0.52. The η_{absorb}, $\eta_{charging}$ and $\eta_{discharging}$ are then equal to 79.6%, 99.2%, and 92.6%, respectively.

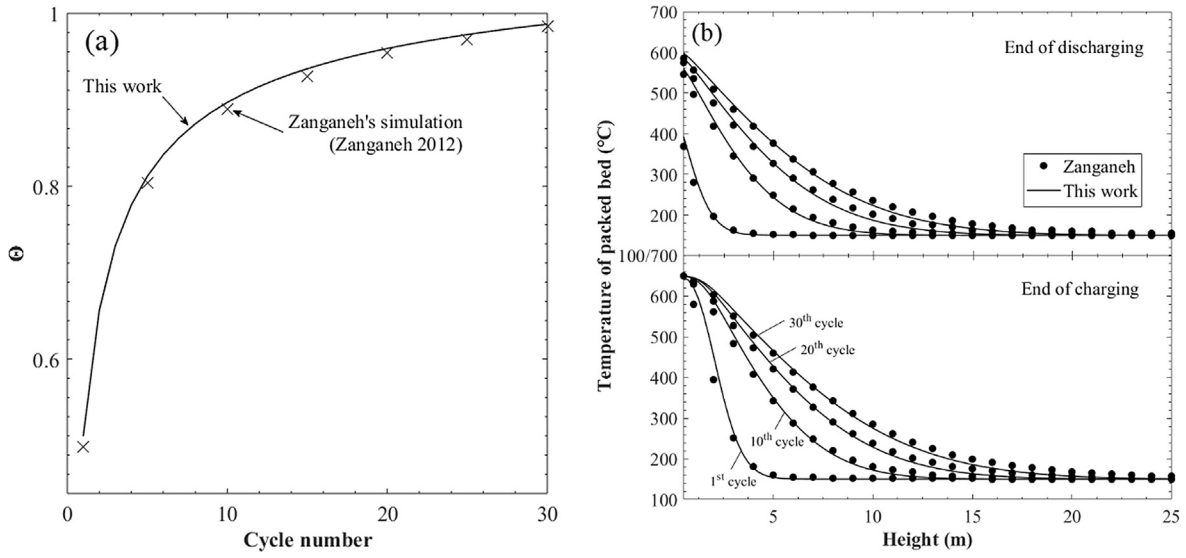

Fig. 3. Validation of the in-house model to Zanganeh (Zanganeh et al., 2012). (a) Nondimensional temperature ($\Theta = \frac{T - T_d}{T_c - T_d}$) of outlet air after each cycle. (b) The solid phase temperature distribution vs height after charging and discharging of 1, 10, 20, and 30 cycles.

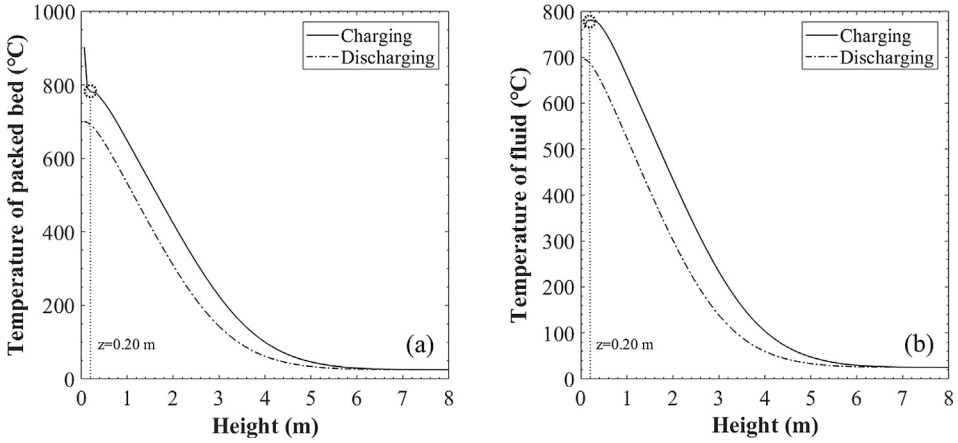

Fig. 4. Thermocline distribution of (a) packed bed, (b) fluid, as the function of temperature vs height after charging\discharging. The equilibrium point (EP) is at $z = 0.20$ m and $T = 781$ °C is marked with a dotted circle in the figure.

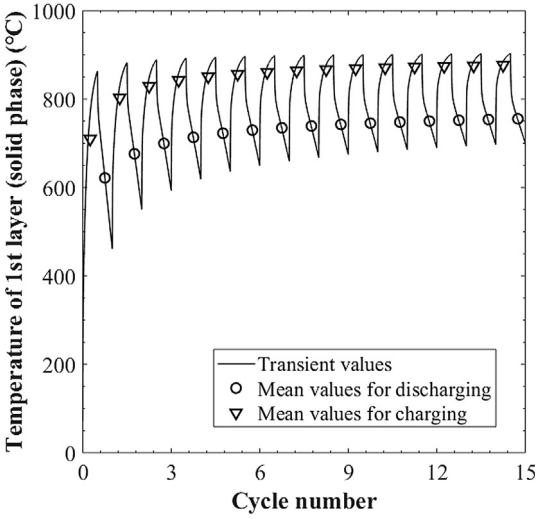

Fig. 5. The temperature evolution of the 1st layer of the packed bed during a multi-cycle simulation.

Table 5
Amount of solar energy absorbed and outlet temperature for the different values of γ and H_3.

γ (H_3 = 0.33 m)	0	2	4	6	8	10
Q_{absorb} (MWh)	2.35	2.77	2.87	2.92	2.95	2.97
$\bar{T}_{outlet}$(°C)	652	735	754	764	770	774
ΔT_{outlet} (°C)	277	160	131	116	107	100

H_3 (m) (γ = 4)	0.33	0.66	0.99	1.32	1.65
Q_{absorb} (MWh)	2.87	2.89	2.89	2.90	2.90
$\bar{T}_{outlet}$(°C)	754	759	760	758	757
ΔT_{outlet} (°C)	131	102	84	77	74

The energy needed for the air fans (Q_{fans}) is calculated in Eq. (27). The derivative of the pressure versus height in the packed bed ($\frac{dp}{dz}$) refers to the Ergun equation (Ergun and Orning, 1949) modified with a buoyancy term (Andersen, 2003). The results indicate that Q_{fans} is an order of magnitude lower than the thermal heat loss though the walls. Hence, it can be neglected in the analysis.

$$Q_{fans} = \frac{\int_0^{t_c+t_d}\int_0^{H_2}\left|\frac{dp}{dz}\right|\frac{\dot{m}}{\rho_f}dzdt}{\eta_{fan}\cdot\eta_{CSP}} \quad (27)$$

4.4. Comparison of receiver and storage to existing CSP plants

Finally, we compares our IRS to the existing CSP plants: the Solar One in California (Kolb et al., 1991), the 100 MWh_{th} TES system in Ait Baha (Zanganeh et al., 2014c), and the CSPonD in Masdar (Gil et al., 2017), based on our results. The comparison is done against η_{absorb}, $\eta_{charging}$, $\eta_{discharging}$, and ξ_{cycle} shown in Table 6. Similar to our case, these three plants employed a thermocline single-tank for the storage design. We found that the IRS performs well and has actually the highest absorbing efficiency and solar-to-exergy conversion ratio as well as a good storage efficiency ($\eta_{storage} = \eta_{charging}\cdot\eta_{discharging}$).

The advantages of the modified IRS receiver and storage compared to existing CSP systems can be summarized as follows:

- Direct absorption of the solar irradiation is more efficient;
- The structure of IRS is simplified by eliminating the conventional receiver, storage system and heat exchanger;
- During charging, the descending airflow formed in the cavity can prevent the convective heat loss through the aperture;
- A higher temperature (> 700 °C) is achieved enabling the use of more efficient thermal engines, e.g. the Brayton or Stirling cycles;
- Circulation air flow can improve the heat transfer rate, uniform the temperature distribution in the upper part thus improving the attenuation of outlet temperature during discharging;

5. Conclusions

In this paper, we proposed a modified integrated receiver-storage (IRS) system for a beam-down CSP plant. The structure is based on a cylindrical packed rock-bed storage. Unlike conventional designs, the IRS can directly store solar irradiation without a complicated heat exchange mechanism which leads to a much simplified structure. We developed a combined thermal model for cavity radiation and storage charging-discharging processes which was used in the thermal analysis indicating that the performance of IRS was very satisfying.

The reheating element coupled to the IRS proved to enhance heat transfer in the storage improving the total thermal efficiency by 12%. The outlet temperature gap could be narrowed by a factor of 3 after adding a circulation air fan to the storage, without any major increase in the parasitic losses. The circulation flow ratio and length affect the reheat effect of the IRS. Optimal parameter values for our 450 kW_{th} design were γ = 6 and H_3 = 1 m.

For the optimal case, a mean temperature of 770 °C was reached and the output temperature gap was within 68 °C. No temperature attenuation phenomenon was observed during the later period of discharging. The solar-to-exergy conversion ratio of the IRS (0.52) can be

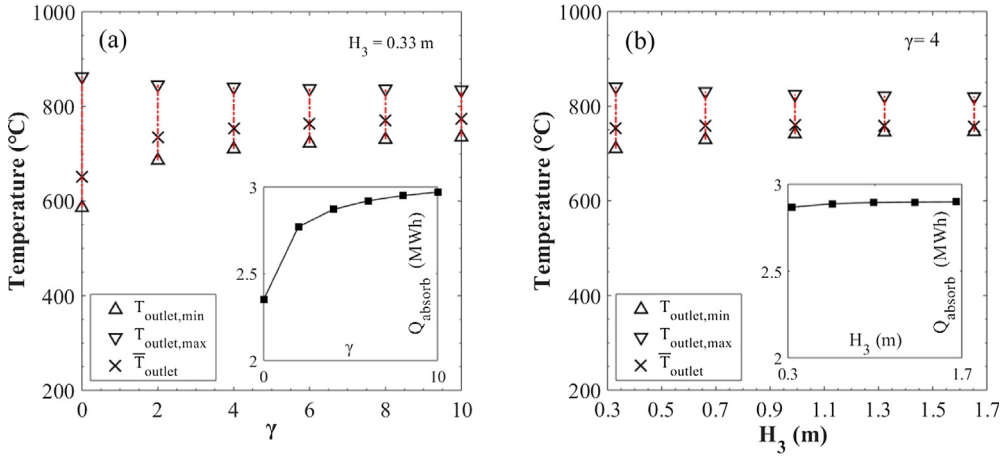

Fig. 6. Effects on outlet temperature ($T_{outlet,\min}$, $T_{outlet,\max}$, $\bar{T}_{outlet}$) and the absorbed amount of solar heat (Q_{absorb}) during the discharging phase of the 30th cycle by varying (a) circulation flow ratio, γ; (b) circulation flow length, H_3;. The dashed red line depicts the gap between the maximum and the minimum outlet temperature (ΔT_{outlet}).

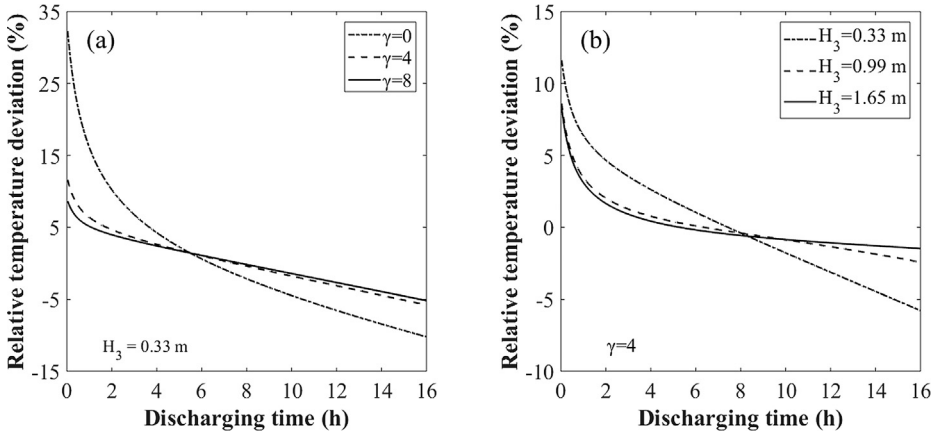

Fig. 7. The relative temperature deviation (σ_T) during discharging of the 30th cycle under the fixed conditions: (a) H_3 = 0.33 m, (b) γ = 4.

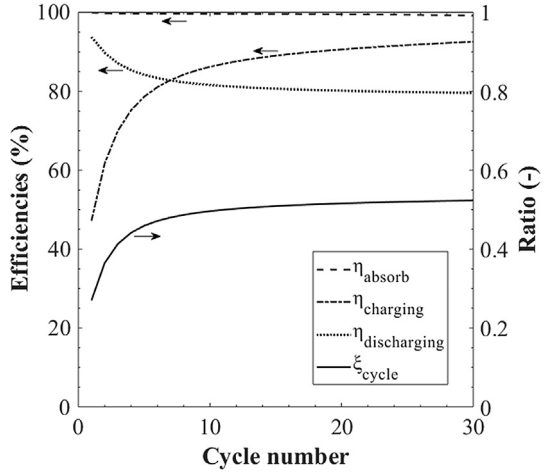

Fig. 8. Thermal efficiencies and solar-to-exergy conversion ratio during a month of operation with γ = 6, H_3 = 1 m.

considered good.

The modified IRS shown in this paper is a promising design for future CSP systems. Further work could include assessing the thermo-mechanical stability, improving the absorbing efficiency of the cavity more and analyzing the feasibility of IRS for high temperature thermochemical reaction systems.

Table 6
Comparison of IRS to three existing CSP systems.

	$\bar{T}_{outlet}$	η_{absorb}	$\eta_{charging}$ / $\eta_{storage}$	$\eta_{discharging}$	ξ_{cycle}
IRS	760 °C	80%	99% 92%	93%	0.52
Solar One (DeLaquil et al., 1991; Kolb et al., 1991)	566 °C	69%	N/A 90%	N/A	0.42
Ait Baha (Zanganeh et al., 2014a; Zanganeh et al., 2014c)	560 °C	77%	98% 89%	91%	0.46
CSPonD (Gil et al., 2017; Slocum et al., 2011)	550 °C	75%	N/A 95.5%	N/A	0.48

Acknowledgements

This work was supported by the National Science Foundation of China (No. 51736006) as well as the Scientific Research Foundation of Graduate School of Southeast University (No. YBPY1855) and Academy of Finland.

References

Alanis, E., Saravia, L., Rovetta, L., 1977. Measurement of rock pile heat transfer coefficients. Sol. Energy 19, 571.

Allen, K., Von Backström, T., Kröger, D., Kisters, A., 2014. Rock bed storage for solar thermal power plants: Rock characteristics, suitability, and availability. Sol. Energy Mater. Sol. Cells 126, 170–183.

Andersen, K.T., 2003. Theory for natural ventilation by thermal buoyancy in one zone with uniform temperature. Build. Environ. 38 (11), 1281–1289.
Becattini, V., 2018. Combined Sensible/Latent Thermal-Energy Storage: Filler Materials, Feasibility at the Pilot Scale, and Design Method. ETH Zurich.
Beek, J., 1962. Design of packed catalytic reactors. Adv. Chem. Eng. 3, 203–271.
Brosseau, D., Kelton, J.W., Ray, D., Edgar, M., Chisman, K., Emms, B., 2005. Testing of thermocline filler materials and molten-salt heat transfer fluids for thermal energy storage systems in parabolic trough power plants. J. Sol. Energy Eng. 127 (1), 109–116.
Chueh, W.C., Falter, C., Abbott, M., Scipio, D., Furler, P., Haile, S.M., Steinfeld, A., 2010. High-flux solar-driven thermochemical dissociation of CO2 and H2O using non-stoichiometric ceria. Science 330 (6012), 1797–1801.
Coutier, J.P., Farber, E., 1982. Two applications of a numerical approach of heat transfer process within rock beds. Sol. Energy 29 (6), 451–462.
DanielsFans, Model AFP – Axial Flow Plug Fan, Available at: https://www.danielsfans.com/high-temperature-fans/axial-fans/model-afp/.
DeLaquil, P., Kelly, B., Lessley, R., 1991. Solar one conversion project. Solar Energy Mater. 24 (1–4), 151–161.
Ergun, S., Orning, A.A., 1949. Fluid flow through randomly packed columns and fluidized beds. Ind. Eng. Chem. 41 (6), 1179–1184.
Flueckiger, S., Yang, Z., Garimella, S.V., 2011. An integrated thermal and mechanical investigation of molten-salt thermocline energy storage. Appl. Energy 88 (6), 2098–2105.
Foamglas Insulation Systems.
Furler, P., Steinfeld, A., 2015. Heat transfer and fluid flow analysis of a 4 kW solar thermochemical reactor for ceria redox cycling. Chem. Eng. Sci. 137, 373–383.
Ganesan, K., Lipiński, W., 2011. Experimental determination of spectral transmittance of porous cerium dioxide in the range 900–1700 nm. J. Heat Transfer 133 (10), 104501.
Geissbühler, L., Kolman, M., Zanganeh, G., Haselbacher, A., Steinfeld, A., 2016. Analysis of industrial-scale high-temperature combined sensible/latent thermal energy storage. Appl. Therm. Eng. 101, 657–668.
Gil, A., Grange, B., Perez, V.G., Tetreault-Friend, M., Codd, D.S., Calvet, N., Slocum, A.S., 2017. CSPonD demonstrative project: Start-up process of a 25 kW prototype. In: AIP Conference Proceedings. AIP Publishing, p. 110003.
Gil, A., Medrano, M., Martorell, I., Lázaro, A., Dolado, P., Zalba, B., Cabeza, L.F., 2010. State of the art on high temperature thermal energy storage for power generation. Part 1—Concepts, materials and modellization. Renew. Sustain. Energy Rev. 14 (1), 31–55.
Herrmann, U., Kearney, D.W., 2002. Survey of thermal energy storage for parabolic trough power plants. J. Sol. Energy Eng. 124 (2), 145–152.
Hischier, I., Leumann, P., Steinfeld, A., 2012. Experimental and numerical analyses of a pressurized air receiver for solar-driven gas turbines. J. Sol. Energy Eng. 134 (2), 021003.
Ismail, K., Stuginsky Jr, R., 1999. A parametric study on possible fixed bed models for PCM and sensible heat storage. Appl. Therm. Eng. 19 (7), 757–788.
Kalogirou, S.A., 2012. A detailed thermal model of a parabolic trough collector receiver. Energy 48 (1), 298–306.
Kaviany, M., 2012. Principles of Heat Transfer in Porous Media. Springer Science & Business Media.
Keene, D.J., Davidson, J.H., LipiĹ, W., 2013. A model of transient heat and mass transfer in a heterogeneous medium of ceria undergoing nonstoichiometric reduction. J. Heat Transfer 135 (5), 052701.
Kelley, K.K., 1960. High-temperature heat-content, heat-capacity, and entropy data for the elements and inorganic compounds. US Bureau of Mines Bull. 584, 232.
Koepf, E., Advani, S.G., Steinfeld, A., Prasad, A.K., 2012. A novel beam-down, gravity-fed, solar thermochemical receiver/reactor for direct solid particle decomposition: Design, modeling, and experimentation. Int. J. Hydrogen Energy 37 (22), 16871–16887.
Kolb, G.J., Alpert, D.J., Lopez, C.W., 1991. Insights from the operation of Solar One and their implications for future central receiver plants. Sol. Energy 47 (1), 39–47.
Kolb, G.J., Lee, G., Mijatovic, P., Valmianski, E., 2011. Thermal Ratcheting Analysis of Advanced Thermocline Energy Storage Tanks. Sandia National Lab.(SNL-NM), Albuquerque, NM (United States).
Kunii, D., Smith, J., 1960. Heat transfer characteristics of porous rocks. AIChE J. 6 (1), 71–78.
Kunii, D., Smith, J., 1961. Heat transfer characteristics of porous rocks: II. Thermal conductivities of unconsolidated particles with flowing fluids. AIChE J. 7 (1), 29–34.
Kuravi, S., Trahan, J., Goswami, D.Y., Rahman, M.M., Stefanakos, E.K., 2013. Thermal energy storage technologies and systems for concentrating solar power plants. Prog. Energy Combust. Sci. 39 (4), 285–319.
Liu, M., Tay, N.S., Bell, S., Belusko, M., Jacob, R., Will, G., Saman, W., Bruno, F., 2016. Review on concentrating solar power plants and new developments in high temperature thermal energy storage technologies. Renew. Sustain. Energy Rev. 53, 1411–1432.
Löf, G., Hawley, R., 1948. Unsteady-state heat transfer between air and loose solids. Ind. Eng. Chem. 40 (6), 1061–1070.
Martinola, G., Meda, A., Plizzari, G.A., Rinaldi, Z., 2010. Strengthening and repair of RC beams with fiber reinforced concrete. Cem. Concr. Compos. 32 (9), 731–739.
Matsubara, K., Kazuma, Y., Sakurai, A., Suzuki, S., Soon-Jae, L., Kodama, T., Gokon, N., Seok, C.H., Yoshida, K., 2014. High-temperature fluidized receiver for concentrated solar radiation by a beam-down reflector system. Energy Procedia 49, 447–456.
Medrano, M., Gil, A., Martorell, I., Potau, X., Cabeza, L.F., 2010. State of the art on high-temperature thermal energy storage for power generation. Part 2—Case studies. Renew. Sustain. Energy Rev. 14 (1), 56–72.
Meier, A., Winkler, C., Wuillemin, D., 1991. Experiment for modelling high temperature rock bed storage. Solar Energy Mater. 24 (1–4), 255–264.
Mokhtar, M., Meyers, S.A., Armstrong, P.R., Chiesa, M., 2014. Performance of a 100 kWth concentrated solar beam-down optical experiment. J. Sol. Energy Eng. 136 (4), 041007.
Ofuchi, K., Kunii, D., 1965. Heat-transfer characteristics of packed beds with stagnant fluids. Int. J. Heat Mass Transf. 8 (5), 749–757.
Pardo, P., Deydier, A., Anxionnaz-Minvielle, Z., Rougé, S., Cabassud, M., Cognet, P., 2014. A review on high temperature thermochemical heat energy storage. Renew. Sustain. Energy Rev. 32, 591–610.
Pelay, U., Luo, L., Fan, Y., Stitou, D., Rood, M., 2017. Thermal energy storage systems for concentrated solar power plants. Renew. Sustain. Energy Rev. 79, 82–100.
Petrasch, J., Wyss, P., Steinfeld, A., 2007. Tomography-based Monte Carlo determination of radiative properties of reticulate porous ceramics. J. Quant. Spectrosc. Radiat. Transfer 105 (2), 180–197.
Pfeffer, R., 1964. Heat and mass transport in multiparticle systems. Ind. Eng. Chem. Fundam. 3 (4), 380–383.
Rabl, A., 1976. Tower reflector for solar power plant. Sol. Energy 18, 269–271.
Riaz, M., 1977. Rock bed heat accumulators. Final report. Minnesota Univ, Minneapolis (USA).
Romero, M., Steinfeld, A., 2012. Concentrating solar thermal power and thermochemical fuels. Energy Environ. Sci. 5 (11), 9234–9245.
Segal, A., Epstein, M., 1999. Comparative performances oftower-top'andtower-reflector'central solar receivers. Sol. Energy 65 (4), 207–226.
Segal, A., Epstein, M., 2001. The optics of the solar tower reflector. Sol. Energy 69, 229–241.
Slocum, A.H., Codd, D.S., Buongiorno, J., Forsberg, C., McKrell, T., Nave, J.-C., Papanicolas, C.N., Ghobeity, A., Noone, C.J., Passerini, S., 2011. Concentrated solar power on demand. Sol. Energy 85 (7), 1519–1529.
Somerton, W.H., 1992. Thermal Properties and Temperature-Related Behavior of Rock/Fluid Systems. Elsevier.
Steinmann, W.-D., Eck, M., 2006. Buffer storage for direct steam generation. Sol. Energy 80 (10), 1277–1282.
Tamaura, Y., Utamura, M., Kaneko, H., Hasuike, H., Domingo, M., Relloso, S., 2006. A novel beam-down system for solar power generation with multi-ring central reflectors and molten salt thermal storage. In: Proceedings of the 13th International Symposium on Concentrating Solar Power and Chemical Energy Technologies, Seville, Spain.
Tamme, R., Laing, D., Steinmann, W.-D., 2004. Advanced thermal energy storage technology for parabolic trough. J. Sol. Energy Eng. 126 (2), 794–800.
Tiskatine, R., Eddemani, A., Gourdo, L., Abnay, B., Ihlal, A., Aharoune, A., Bouirden, L., 2016. Experimental evaluation of thermo-mechanical performances of candidate rocks for use in high temperature thermal storage. Appl. Energy 171, 243–255.
ToolBox, E., 2005. Dry Air Properties.
Vant-Hull, L., 2014. Issues with beam-down concepts. Energy Procedia 49, 257–264.
Wei, X., Lu, Z., Yu, W., Xu, W., 2013. Ray tracing and simulation for the beam-down solar concentrator. Renew. Energy 50, 161–167.
Whitaker, S., 1972. Forced convection heat transfer correlations for flow in pipes, past flat plates, single cylinders, single spheres, and for flow in packed beds and tube bundles. AIChE J. 18 (2), 361–371.
Yagi, S., Kunii, D., 1957. Studies on effective thermal conductivities in packed beds. AIChE J. 3 (3), 373–381.
Yang, S., Wang, J., Lund, P.D., Jiang, C., Huang, B., 2018. Design and performance evaluation of a high-temperature cavity receiver for a 2-stage dish concentrator. Sol. Energy 174, 1126–1132.
Zanganeh, G., Ambrosetti, G., Pedretti, A., Zavattoni, S., Barbato, M., Good, P., Haselbacher, A., Steinfeld, A., 2014a. A 3 MWth parabolic trough CSP plant operating with air at up to 650 °C. In: 2014 International renewable and sustainable energy conference (IRSEC). IEEE, pp. 108–113.
Zanganeh, G., Commerford, M., Haselbacher, A., Pedretti, A., Steinfeld, A., 2014b. Stabilization of the outflow temperature of a packed-bed thermal energy storage by combining rocks with phase change materials. Appl. Therm. Eng. 70 (1), 316–320.
Zanganeh, G., Khanna, R., Walser, C., Pedretti, A., Haselbacher, A., Steinfeld, A., 2015a. Experimental and numerical investigation of combined sensible–latent heat for thermal energy storage at 575 C and above. Sol. Energy 114, 77–90.
Zanganeh, G., Pedretti, A., Haselbacher, A., Steinfeld, A., 2015b. Design of packed bed thermal energy storage systems for high-temperature industrial process heat. Appl. Energy 137, 812–822.
Zanganeh, G., Pedretti, A., Zavattoni, S., Barbato, M., Haselbacher, A., Steinfeld, A., 2014c. Design of a 100 MWhth packed-bed thermal energy storage. Energy Procedia 49, 1071–1077.
Zanganeh, G., Pedretti, A., Zavattoni, S., Barbato, M., Steinfeld, A., 2012. Packed-bed thermal storage for concentrated solar power–Pilot-scale demonstration and industrial-scale design. Sol. Energy 86 (10), 3084–3098.
Zavattoni, S.A., Barbato, M.C., Pedretti, A., Zanganeh, G., 2015. Single-tank TES system–Transient evaluation of thermal stratification according to the second-law of thermodynamics. Energy Procedia 69, 1068–1077.